



Poly(ionic liquid)-based bimetallic tandem catalysts for highly efficient carbon dioxide electroreduction

Xiao-Qiang Li^{a,b}, Guo-Yi Duan^{a,*}, Rui Wang^{a,c}, Li-Jun Han^a, Yao-Feng Wang^{a,b}, Bao-Hua Xu^{a,b,**}

^a Beijing Key Laboratory of Ionic Liquids Clean Process, CAS Key Laboratory of Green Process and Engineering, State Key Laboratory of Multiphase Complex Systems, Institute of Process Engineering, Chinese Academy of Sciences, Beijing 100190, China

^b School of Chemical Engineering, University of Chinese Academy of Sciences, Beijing 100049, China

^c State Key Laboratory of Chemical Engineering, East China University of Science and Technology, Shanghai 200237, China

ARTICLE INFO

Keywords:

CO₂ conversion
Electrocatalysis
Organic-inorganic hybrids
Ionic liquids
Electrolysis

ABSTRACT

Poly(ionic liquid)-metal (PIL-metal) hybrids were developed as a platform for facilely constructing tandem catalysts to reach highly efficient electrocatalytic reduction of CO₂ (CO₂RR). By introducing extra metal with distinct CO₂RR response to Cu-PIL hybrids, Cu@PIL@Ag and Cu@PIL@Bi were obtained. Remarkably, Cu@PIL@Ag exhibits an excellent C₂₊ Faradaic efficiency (FE_{C2+}) of 83.2% with a high partial current density (j_{C2+}) of 416.1 mA cm⁻² in 3 M KOH and an even higher j_{C2+} (708.9 mA cm⁻²) in 1 M KOH, while Cu@PIL@Bi possesses high FE_{C1} (> 60%) and low FE_{C2+} (< 5%) in a wide potential range. Mechanistic studies demonstrate the output of such a tandem system, either synergistic or maladjusted, depends on not only CO₂RR response of Ag and Bi but also specific Cu-Ag and Cu-Bi interactions. Besides, the PIL layer could adjust the reactivity by promoting the dispersion and availability of active sites and enriching the local key intermediates.

1. Introduction

Electrochemical CO₂ reduction reaction (CO₂RR) has attracted extensive research interest due to the increasing availability of renewable electricity in recent years [1,2]. By adopting such a sustainable and green route, high value-added chemicals can be produced under mild conditions (i.e., at ambient temperature and/or ambient pressure) while realizing the recycling of greenhouse gas [3–5]. Previous studies have shown the CO₂RR consists of complicated multi-step pathways and involves a variety of intermediates [6,7]. The selectivity regulation of the reduction products of CO₂RR, especially that toward high-value multi-electron reduction (> 2e⁻) products, at high current density remains a challenge. Despite numerous strategies that have been achieved in this field, the tandem catalysis of decoupling CO₂RR into continuous reactions at different active sites by taking the key intermediate as the “boundary” promises a high product selectivity.

The tandem catalysts by regulating the formation of CO are the most explored since the local concentration of *CO intermediates could adjust

the selectivity and distribution of C₂₊ product based on the C–C coupling mechanism [8]. For instance, Yang's group employed physically mixed Cu and Ag nanoparticles (NPs) as a highly efficient (Cu-Ag) tandem catalyst, which provided a high FE_{C2+} of ~45% at high rates (~180 mA cm⁻²) [9]. In the study, they demonstrated the CO-enriched local environment caused by silver moiety promotes the formation of C₂₊ products on copper moiety. Hahn and Jaramillo jointly deposited Au NPs on a polycrystalline Cu foil to prepare a Cu-Au tandem catalyst, which exhibited over 100 times selectivity toward C₂₊ products than CH₄ or CH₃OH [10]. Combined electrochemical tests and transport modeling suggest that the reduction of CO₂ on Au creates a high CO concentration near the Cu sites, where CO is further reduced to C₂₊ products under locally alkaline conditions. Sun and Wu jointly reported that a high C₂₊ selectivity of 74% was obtained on a CuO-ZnO tandem catalyst [11]. The partial current density was high (j_{C2+} = 271.6 mA cm⁻²). During the electrolysis, the extra CO formed on the reduced ZnO NPs could increase the surface coverage of *CO on the reduced CuO NPs, thus promoting the C–C coupling reaction.

* Corresponding author.

** Corresponding author at: Beijing Key Laboratory of Ionic Liquids Clean Process, CAS Key Laboratory of Green Process and Engineering, State Key Laboratory of Multiphase Complex Systems, Institute of Process Engineering, Chinese Academy of Sciences, Beijing 100190, China.

E-mail addresses: duanguoyi@ipe.ac.cn (G.-Y. Duan), bhxxu@ipe.ac.cn (B.-H. Xu).

<https://doi.org/10.1016/j.apcatb.2022.121459>

Received 1 February 2022; Received in revised form 6 April 2022; Accepted 25 April 2022

Available online 28 April 2022

0926-3373/© 2022 Elsevier B.V. All rights reserved.

Meanwhile, the C_1 selectivity can also be improved by employing the tandem strategy. Bao's group found that CH_4 was produced at a high reaction rate of 44.3 mA cm^{-2} on the cobalt phthalocyanine (CoPc) and zinc–nitrogen–carbon (Zn–N–C) tandem catalyst [12]. Mechanistic studies demonstrated that CoPc enhanced the availability of both *CO and *H over Zn–N₄ sites leading to a high partial current density of CH_4 generation. A recent research showed that a full selectivity toward CO can be reached on a Cu-based tandem catalyst, which consists of single Cu sites coordinated with both N and S anchored carbon matrix and high-dispersed Cu clusters ($Cu-S_1N_3/Cu_x$) [13]. In addition to the appropriate binding energy for the *COOH intermediate by the $Cu-S_1N_3$ sites, the accelerated *H supply from Cu_x sites also accounts for the outstanding performance of such a catalyst. Further, the introduced second metal (Bi) could promote the CO_2RR performance by electronic modulation of both adjacent Cu sites and the key intermediate as well as accelerating the electron transfer from active sites to reaction species [14].

Various approaches have been developed to provide the tandem catalyst, including physical method [9,10,12,15], galvanic replacement reaction (GRR) [16,17], seed-mediated method [18], chemical reduction [19], electrochemical reduction [20], co-precipitation [11], and pyrolysis [13]. It's fundamental to link different active sites together tightly and uniformly and maintain the overall conductivity of the material for a tandem electrocatalyst. To obtain efficient structure by high throughput screening and systematically study the tandem effects of CO_2RR , a facile and universal preparation strategy is urgent. Recently, our team reported a type of novel poly(ionic liquid)-Cu NPs (Cu@PIL) hybrids [21], wherein the abundant imidazolium-pyridinic-imidazolium chelate sites and interlaced anions networks in the PIL shell enable the immobilization of other metal elements to the copper surface by simple impregnation. As a proof of concept, the representative active sites of Pd (for CO_2 -to- CO) and Cu (for C–C coupling) were introduced to the neighbor of Cu NPs by impregnating Cu@PIL with the corresponding metal salts, thereby respectively delivering Cu–Pd (Cu@PIL@Pd) and Cu–Cu (Cu@PIL@Cu) tandem catalysts [22,23]. Under the optimum conditions, both exhibited remarkable enhancement in the FE_{C_2+} (Cu@PIL@Pd: 178.3 mA cm^{-2} , 68.7% FE_{C_2+} [22]; Cu@PIL@Cu: 304.2 mA cm^{-2} , 76.1% FE_{C_2+} [23]) as compared to the pristine Cu@PIL (174.0 mA cm^{-2} , 58.0% FE_{C_2+} [21]). In addition to the synergy effect obtained by the Cu NPs, the dispersed second metal element, the in-situ generated phases, and the PIL layer significantly contributes to the distinct feature of such tandem catalysts. Meanwhile, the increased local concentration of CO_2 by specific functional groups near the active site could boost the formation of key intermediates during CO_2RR [24]. The advantage of the PIL layer on the CO_2RR was summarized including: (i) the PIL layer functions as a medium, which facilitates the dispersion of active sites, benefitted from abundant tridentate sites and electrostatic network therein; (ii) the diffusion of the in-situ formed *CO is suppressed by the PIL layer, enriching the local CO concentration for the subsequent hydrogenation and C–C coupling; and (iii) the distinct morphology (high specific area and porosity) and interlaced electrostatic network (especially when more metal cations were introduced) of PIL layer enhance not only the availability of active sites but also the conductivity of the catalysts, which could improve the reaction rate of CO_2RR process. These characteristics make the metal-PIL hybrid a promising platform for studying the tandem CO_2RR strategy.

Herein, to obtain more insights on the metal-PIL hybrid-based tandem systems and develop highly efficient CO_2RR catalysts, both elements of Ag and Bi featuring with the CO-selectivity [9] and $HCOOH$ -selectivity [25] for the CO_2RR process, respectively, were introduced into the Cu-PIL hybrid. Besides, chloride ion was employed as the counter ion of PIL layer because Cu@PIL with chloride ion exhibited high C_{2+} selectivity and high reaction rate [21]. Remarkably, by employing Cu@PIL@Ag, a high FE_{C_2+} of 71.5% was achieved with a very high j_{C_2+} of 708.9 mA cm^{-2} at the cathodic potential ($E_{cathodic}$) of -1.69 V (with respect to the reversible hydrogen electrode (RHE), the

same below) in alkaline electrolyte solution (1 M KOH). Further, an even higher FE_{C_2+} of 83.2% (with j_{C_2+} of 416.1 mA cm^{-2}) was obtained in 3 M KOH by the galvanostatic method. By contrast, Cu@PIL@Bi possesses high FE_{C_1} ($> 60\%$) in a wide $E_{cathodic}$ range of -0.70 V to -1.20 V . Mechanistic studies revealed that the introduced Ag and Bi elements do correspond to the specific intermediates, namely CO and $HCOOH$, respectively. Furthermore, the different CO_2RR responses of Ag and Bi, the respective Ag–Cu interaction (with electron transfer) and Bi–Cu interaction (without electron transfer), and the influence of the PIL layer, in combination lead to the distinct CO_2RR performance on such two bimetallic tandem catalysts.

2. Experimental

2.1. Synthesis of Cu@PIL@M (M = Ag and Bi)

The Cu@PIL was synthesized according to our previous work [21]. In this work, Cu@PIL with chloridion as counter ion was employed. Cu@PIL@M was prepared by impregnating Cu@PIL with silver and bismuth salts. Typically, a suspension of silver acetate (AgOAc, 0.134 g, 0.8 mmol, 0.17 equiv.) in methanol (10 mL) was added to the suspension of Cu@PIL in methanol (50 mL). After refluxing at 50°C for 12 h, the mixture was filtrated and rinsed by methanol ($30 \text{ mL} \times 5$). Then it was dried at 60°C for 12 h to afford Cu@PIL@Ag. For Cu@PIL@Bi, a suspension of $BiCl_3$ (0.252 g, 0.8 mmol, 0.17 equiv.) in methanol (10 mL) was added to the suspension of Cu@PIL.

2.2. Synthesis of PIL@M (M = Ag and Bi)

The synthesis of PIL@M is similar, in which silver and bismuth salts were added to PIL without Cu NPs. Theoretically, the dosage should be the same as above. However, the CO_2RR performances of the obtained catalysts were quite poor (mainly producing H_2), which should be due to the small number of active sites. Therefore, a higher dosage of silver and bismuth salts was used. Typically, a suspension of AgOAc (0.083 g, 0.5 mmol) in methanol (5 mL) was added to the suspension of PIL (0.434 mg) in methanol (35 mL). After refluxing at 50°C for 12 h, the mixture was filtrated and rinsed by methanol ($30 \text{ mL} \times 5$). Then it was dried at 60°C for 12 h to afford PIL@Ag. For PIL@Bi, a suspension of $BiCl_3$ (0.158 g, 0.5 mmol) in methanol (5 mL) was added.

2.3. Electrochemical tests

The CO_2RR test was conducted in a home-made electrolyzer with thin gas and electrolyte chambers [21]. A piece of gas diffusion electrode (GDE) loaded with catalyst, a piece of Ni foam, and a mercuric oxide electrode were used as the working electrode, the counter electrode, and the reference electrode, respectively. Alkaline electrolyte solution (1 M KOH) and high-purity CO_2 gas were employed as the electrolyte solution and the feed gas, respectively. Gaseous products were detected by an online gas chromatography system, while the liquid products were analyzed by a nuclear magnetic resonance spectrometer. *In-situ* Raman analysis was conducted in a custom-made electrolyzer [21]. A piece of GDE loaded with catalyst, a graphite rod, and a mercuric oxide electrode were employed as the working electrode, the counter electrode, and the reference electrode, respectively. The detailed operation procedures are shown in Section S3 in Supplementary Information.

3. Results and discussion

3.1. Characterizations of Cu@PIL@Ag

The Cu@PIL@Ag catalyst was facilely synthesized by impregnating a proper dosage of silver acetate (AgOAc, 5 mol% compared to Cu NPs) into previously reported Cu@PIL hybrid. Herein, chloride ion was employed as the counter ion due to its ability to promote C_{2+} selectivity

and current density [21,27]. The crystal structure was characterized by X-ray diffraction (XRD) analysis. As shown in Fig. 1a, the intense patterns at the 2 θ degree of 43.3° and 50.4° were assigned to the (111) and (200) planes of metallic Cu, respectively. Besides, in addition to the Cu₂O-related pattern at ~36°, the other three residual patterns can be identified as the (111), (200), and (220) planes of metallic Ag, respectively.

The high-resolution transmission electron microscopy (HR-TEM) image (Figs. 1b and S1a) confirms such crystal structures of Cu@PIL@Ag. By identifying the distinct lattice fringes, the moieties of metallic Cu, Cu₂O, and metallic Ag were well distinguished as highlighted with red, orange, and blue dashed lines, respectively. Evidently, the nano-sized copper and silver species exist in a highly fragmented manner, enabling the creation of many Cu-Ag interfaces. Further, the presence of interfaces between Cu and Ag species was unambiguously demonstrated by the corresponding energy dispersive X-ray (EDX) images (Fig. 1c). Herein, the formation of metallic Ag (Ag(0)) originated from AgOAc (Ag(I)) suggests a redox reaction readily occurs during the impregnation; it signifies the electron transfer from the Cu species to the Ag species. Besides, the Brunauer-Emmett-Teller (BET) test (Fig. S1b) demonstrate the typical micro-mesoporous structure [26] of Cu@PIL@Ag hybrid with high specific areas ($S_{\text{BET}} = 183.79 \text{ m}^2 \text{ g}^{-1}$). After being loaded on the carbon paper-based GDE, the Cu@PIL@Ag material shows aggregated spherical morphology as indicated by the scanning electron microscopy (SEM) image (Fig. 1d). Moreover, the cross-sectional SEM and EDX mapping images (Fig. 1e) demonstrate the porous structure and the highly distributed Cu and Ag elements at the catalyst layer.

X-ray photoelectron spectroscopy (XPS) results of Cu@PIL@Ag were obtained to detect the types of elements and their chemical environment

at the surface (Figs. 2 and S2). XPS survey spectrum (Fig. 2a) shows the intensity of Ag 3d is quite weak because of the small dosage of AgOAc for the synthesis. Besides, the Cu LMM Auger spectrum (Fig. 2b) features typical metallic Cu and Cu₂O at the kinetic energy (KE) of 918.60 eV [27] and 916.30 eV [28], respectively. Compared to the pristine Cu@PIL [21], the intensity of both Cu(0) and Cu(I) species, including metallic Cu (918.70 eV), Cu₂O (916.30 eV), and Cu(I) complexes (~914 eV) [29] decreases, while that of Cu(II) complexes (918.00 eV) [30], is enhanced. As demonstrated in our latest study [23], Cu(I) complexes mainly come from the interfacial interaction between the PIL and the surface of Cu NPs, while Cu(II) complexes should be attributed to the highly dispersed Cu species in the PIL layer. Therefore, the above XPS results indicate a significant reconstruction of the Cu-PIL interface by introducing AgOAc, which should be resulted from the electron transfer from the Cu species to the Ag species.

The presence of metallic Ag was further confirmed by Ag 3d_{5/2} spectrum (Fig. 2c). Notably, in addition to the feature of bulk metallic Ag at the binding energy (BE) of 368.30 eV [31], a much more intense peak at 368.95 eV can be assigned to the Ag(0) in Ag cluster or nano-sized Ag particles (Table S3) [32]. These results demonstrate the metallic Ag presents on the surface of Cu NPs in a highly dispersed status with the size of sub nano- to nano-meters. Meanwhile, the chelated Ag species was also detected locating at the BE of 368.70 eV [33,34]. Besides, both AgCl (368.10 eV) and Ag₂O (367.70 eV) [35] features with low intensity, which suggests AgOAc was slightly confronted with the anion exchange with Cl-based PIL and hydrolysis with moisture. On the other hand, the N 1s XPS spectrum (Fig. 2d) contains two peaks for transition metal-chelated pyridine and carbene species at 399.50 eV and 400.00 eV, respectively [36,37], representing the coordination

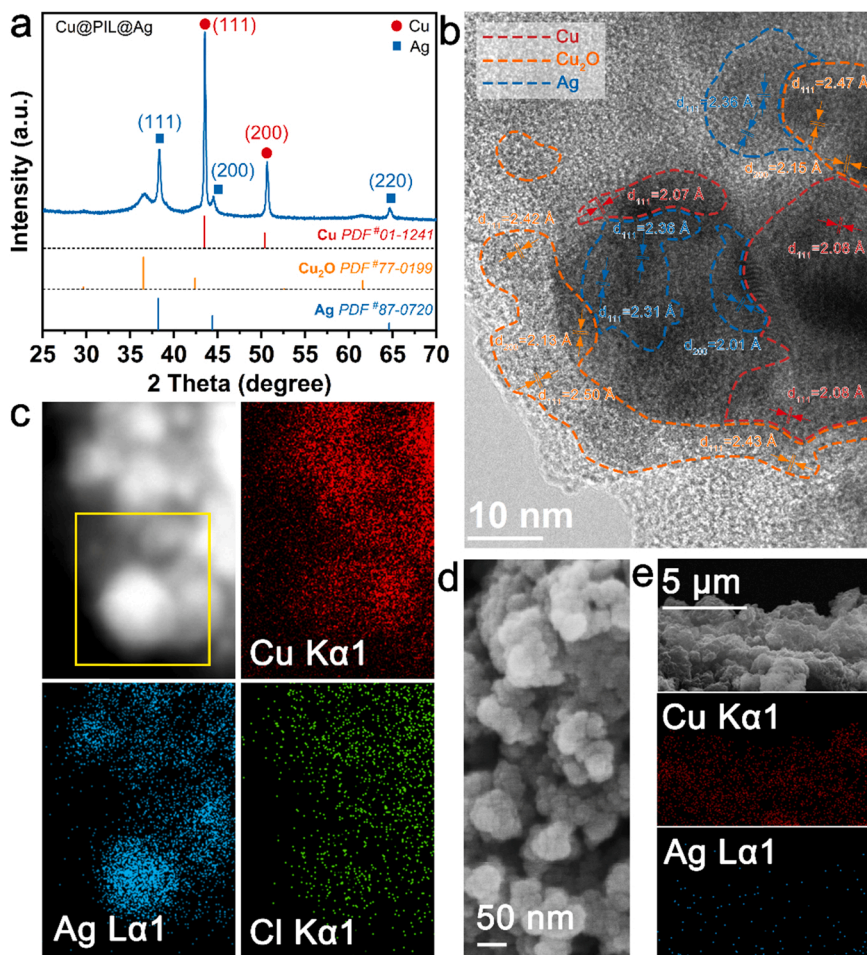


Fig. 1. (a) X-ray diffraction (XRD) patterns of Cu@PIL@Ag. (b) High-resolution transmission electron microscope (HR-TEM) image of Cu@PIL@Ag (red, orange, and blue dashed lines show fragments of metallic Cu, Cu₂O, and metallic Ag, respectively). (c) Energy dispersive x-ray (EDX) mapping images of Cu@PIL@Ag (yellow square in c represents the same region in b). (d-e) Scanning electron microscope (SEM), cross-sectional SEM, and corresponding EDX mapping images of GDE loaded with Cu@PIL@Ag.

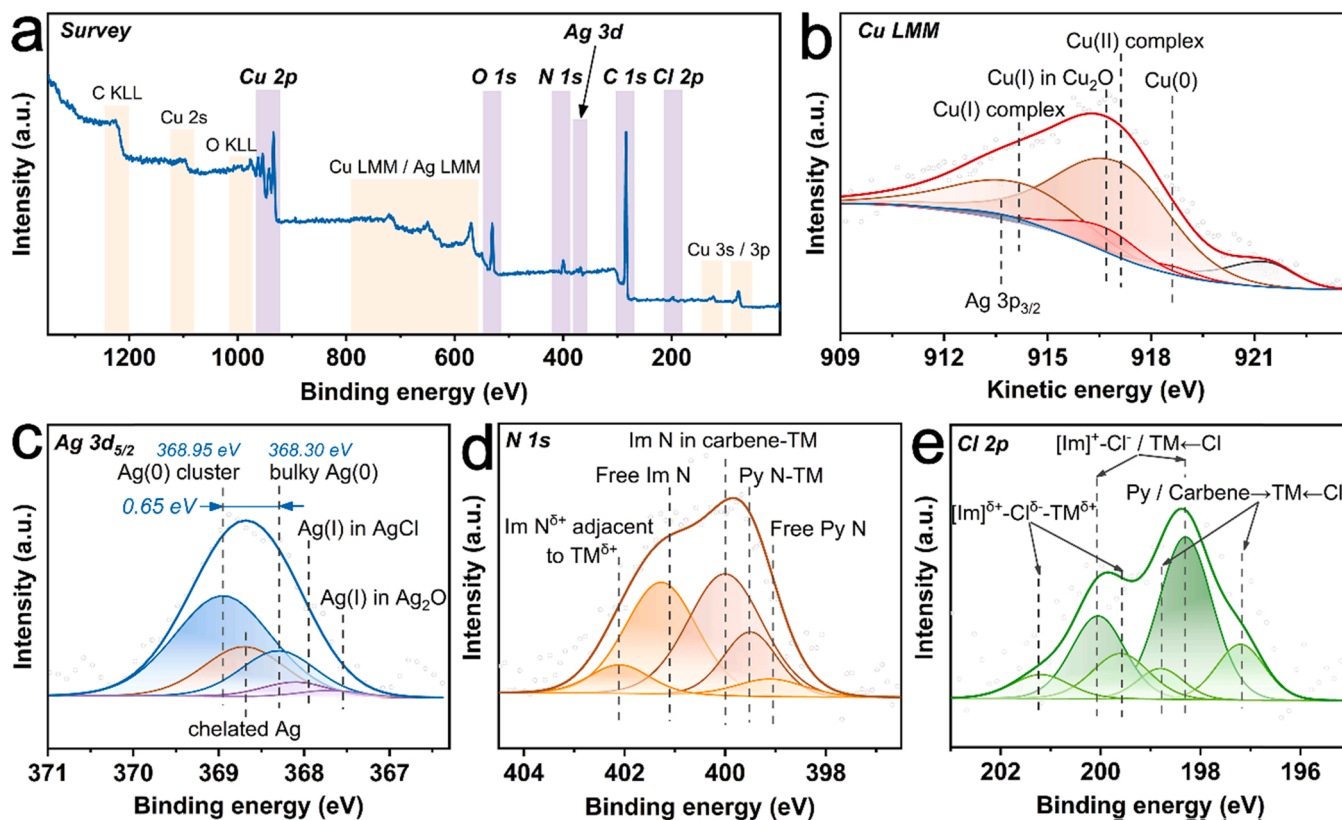


Fig. 2. (a) X-ray photoelectron spectroscopy (XPS) survey spectrum of Cu@PIL@Ag. (b) Cu LMM Auger spectrum of Cu@PIL@Ag. (c-e) High-resolution XPS spectra of Cu@PIL@Ag in Ag 3d_{5/2}, N 1s, and Cl 2p regions. (Im: imidazolium; Py: pyridinic; TM: transition metal).

interaction of the PIL with either Cu or Ag. Further, the peak at 402.1 eV is assigned to the imidazolium nitrogen with less free charges (namely Im N^{δ+}), which embeds in an electrostatic interaction network, Im N^{δ+}... Cl^{δ-}... TM^{δ+}, composed by transition metal cations (including Ag and Cu cations), Cl anions and imidazolium moieties. The Cl 2p XPS spectrum (Fig. 2e) also suggests the presence of chloride sites surrounded by adjacent transition metal cations and imidazolium moieties as demonstrated by the peaks at 199.60 eV and 201.20 eV. In this way, the highly dispersed electrostatic interaction networks can be accessed, which thereby improves the conductivity of the PIL layer.

3.2. Electrocatalytic CO₂RR performance of Cu@PIL@Ag

A home-made flow electrolyzer with separated gas and electrolyte chambers [21] was employed to accelerate the transfer of gaseous reactants. The electrocatalytic CO₂RR performance of Cu@PIL@Ag was first evaluated at different E_{cathodic} (Figs. 3a and S3). When E_{cathodic} negatively shifts from -0.67 V to -1.69 V, the total current density (j_{total}) increases continually from 84.3 mA cm⁻² to 992.0 mA cm⁻². The best j_{total} corresponds to a very high reaction rate reached by Cu@PIL@Ag. Such excellent catalytic CO₂RR activity surpasses those of most other catalysts (Table S8). It's worthy to note that a higher j_{total} (> 1 A cm⁻²) can be accessed at more negative E_{cathodic} by experiments. However, the Joule heating effect becomes significant in this case, resulting in the instability of the whole system.

In addition to the activity (j_{total}), the selectivity of C₂₊ products (FE_{C2+}) also increases with more negative E_{cathodic} . A high FE_{C2+} of 71.5% with a high $j_{\text{C2+}}$ of 708.9 mA cm⁻² was obtained at -1.69 V, which is the best $j_{\text{C2+}}$ record compared to the reported values on tandem catalysts (Table S8). At the same time, the selectivity of C₁ products (FE_{C1}) decreases with negatively shifting E_{cathodic} , signifying an obvious trade-off relationship between the generation of C₁ and C₂₊ products.

This result also suggests the transformation of the in-situ generated CO to multi-carbon compounds with increasing overpotentials since CO is the main C₁ product at relatively positive E_{cathodic} (Figs. S3 and S4).

Both ethanol and ethylene are the major C₂₊ products at all E_{cathodic} , while the selectivity towards ethanol is slightly higher (Fig. 3b and c). As the best result, the faradaic efficiency and partial current density of ethanol are respectively 30.8% and 305.1 mA cm⁻² at -1.69 V, while those of ethylene are 28.1% and 279.0 mA cm⁻² at the same potential. We also noticed that the FE_{H2} was low even at a quite high reaction rate (e.g., FE_{H2} = 17.8% when j_{total} = 992.0 mA cm⁻²), signifying the major side reaction, namely the hydrogen evolution reaction (HER), is effectively suppressed on Cu@PIL@Ag.

Different concentration of KOH solution was used to study the influence of alkalinity (or the OH⁻ concentration) near the surface of electrocatalysts through the galvanostatic method. The FE_{C2+} increases with increasing the concentration of KOH from 0.5 M to 3.0 M (0.5 M, 55.2%; 1.0 M, 61.1%; 3.0 M, 83.2%; Figs. 3d and S5), while FE_{CO} decreases from 28.5% (0.5 M) to 4.5% (3.0 M). It indicates highly alkaline electrolyte solution could promote the C-C coupling of *CO intermediate over Cu@PIL@Ag, which agrees with the previous reports on CO₂RR [38]. We also noticed the FE_{C2+} decreases to 72.2% in 5 M KOH solution (vs. 83.2% in 3 M KOH), while both FE_{C1} (11.2%) and FE_{CO} (3.7%) basically remain (vs. 12.5% and 4.5%, respectively, in 3 M KOH). Therefore, the reduction in FE_{C2+} is most likely owing to that more current was consumed by HER (FE_{H2} = 15.2%) in 5 M KOH electrolyte solution (Fig. S5). The product distribution profile (Fig. 3e) clearly shows that the distribution of the C₂₊ products varies with different alkalinity and the highest FE of liquid C₂₊ products (55.0%) was obtained in 3 M KOH with a high $j_{\text{C2+}}$ of 257.1 mA cm⁻² (Fig. S6).

The long-term stability experiment was conducted in 1 M KOH solution at different current densities (Figs. 3f, g, S7, and S8). At 150 mA cm⁻², the E_{cathodic} (with iR compensation) slightly fluctuates

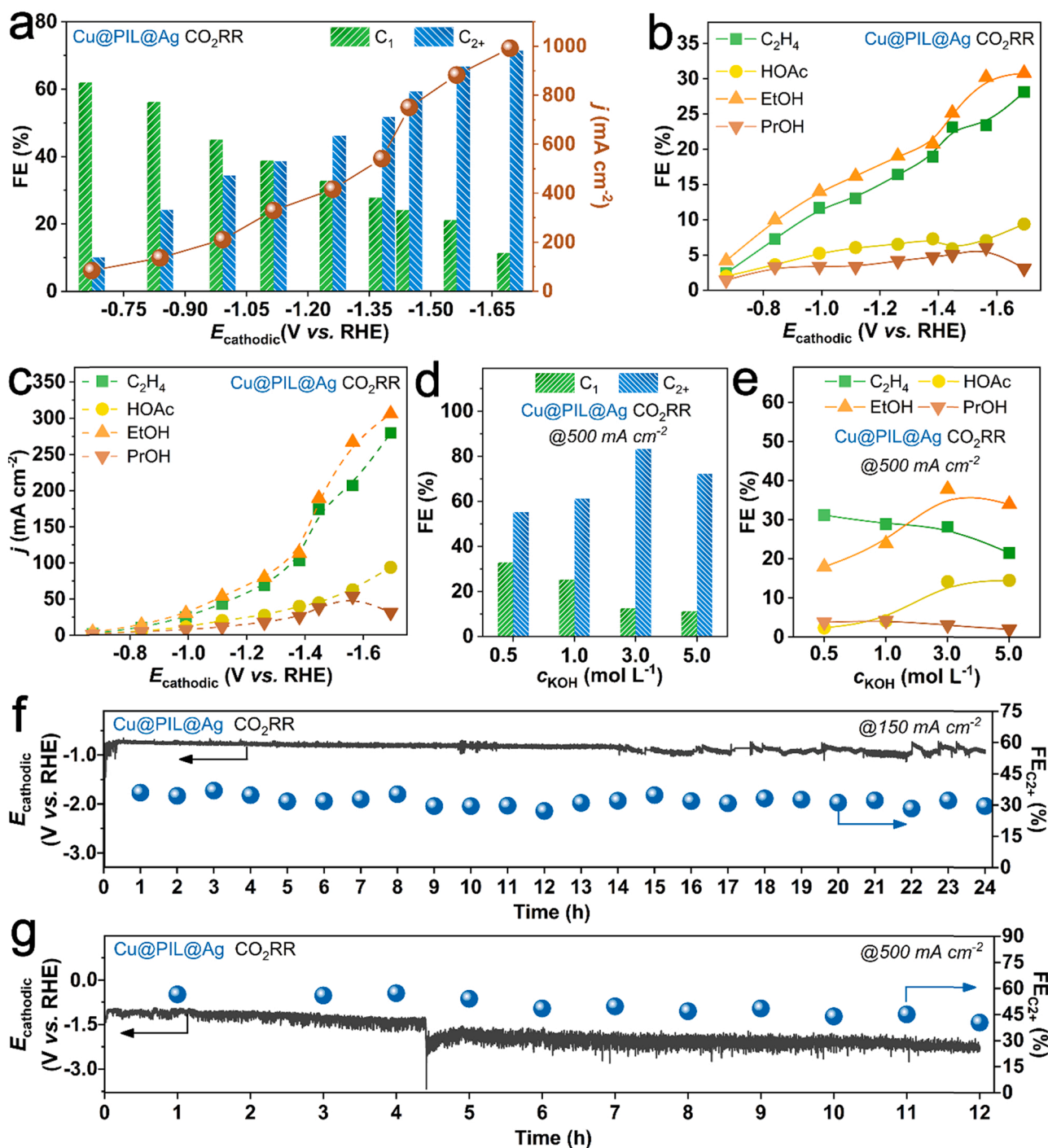


Fig. 3. (a) Electrocatalytic CO₂RR performance of Cu@PIL@Ag in KOH solution (1 M) at different E_{cathodic} . (b-c) Faradaic efficiency (FE) and partial current density (j) of C₂ products on Cu@PIL@Ag in KOH solution (1 M) at different E_{cathodic} . (d) Electrocatalytic CO₂RR performance of Cu@PIL@Ag in KOH solution with different concentrations at 500 mA cm⁻². (e) FE of C₂ products on Cu@PIL@Ag in KOH solution with different concentrations at 500 mA cm⁻². (f-g) Stability test of Cu@PIL@Ag in KOH solution (1 M) at 150 mA cm⁻² for 24 h and 500 mA cm⁻² for 12 h.

between -0.75 V and -0.82 V within the first 14 h (Fig. 3f). It follows by a more intensive fluctuation from -0.75 V to -0.95 V. The selectivity towards C₂ product is around 30% every one hour, thereby an average FE_{C₂+} of 31.9% has been reached for 24-hour long electrolysis. It demonstrates Cu@PIL@Ag electrocatalyst persists good stability. At 500 mA cm⁻², the FE_{C₂+} decreased from 56.3% to 40.5% and the E_{cathodic} negatively shifted from -1.25 V to -2.15 V after 12-hour long electrolysis (Fig. 3g). Similarly, remarkable decrease in FE_{C₂+} (from 74.0% to 43.2%) was observed within 3 h by further increasing the current density to 1000 mA cm⁻² (Fig. S7). Such attenuation of

electrocatalytic performance at high current densities could be attributed to the severe flooding and carbonation of the microporous layer of GDE since the OH⁻ was significantly accumulated at high reaction rates.

3.3. Characterizations and electrocatalytic CO₂RR performance of Cu@PIL@Bi

Cu@PIL@Bi was prepared in a similar way to Cu@PIL@Ag, in which bismuth trichloride (BiCl₃, 5 mol% compared to Cu NPs) was introduced as the bismuth source. XRD patterns in Fig. 4a clearly show the metallic

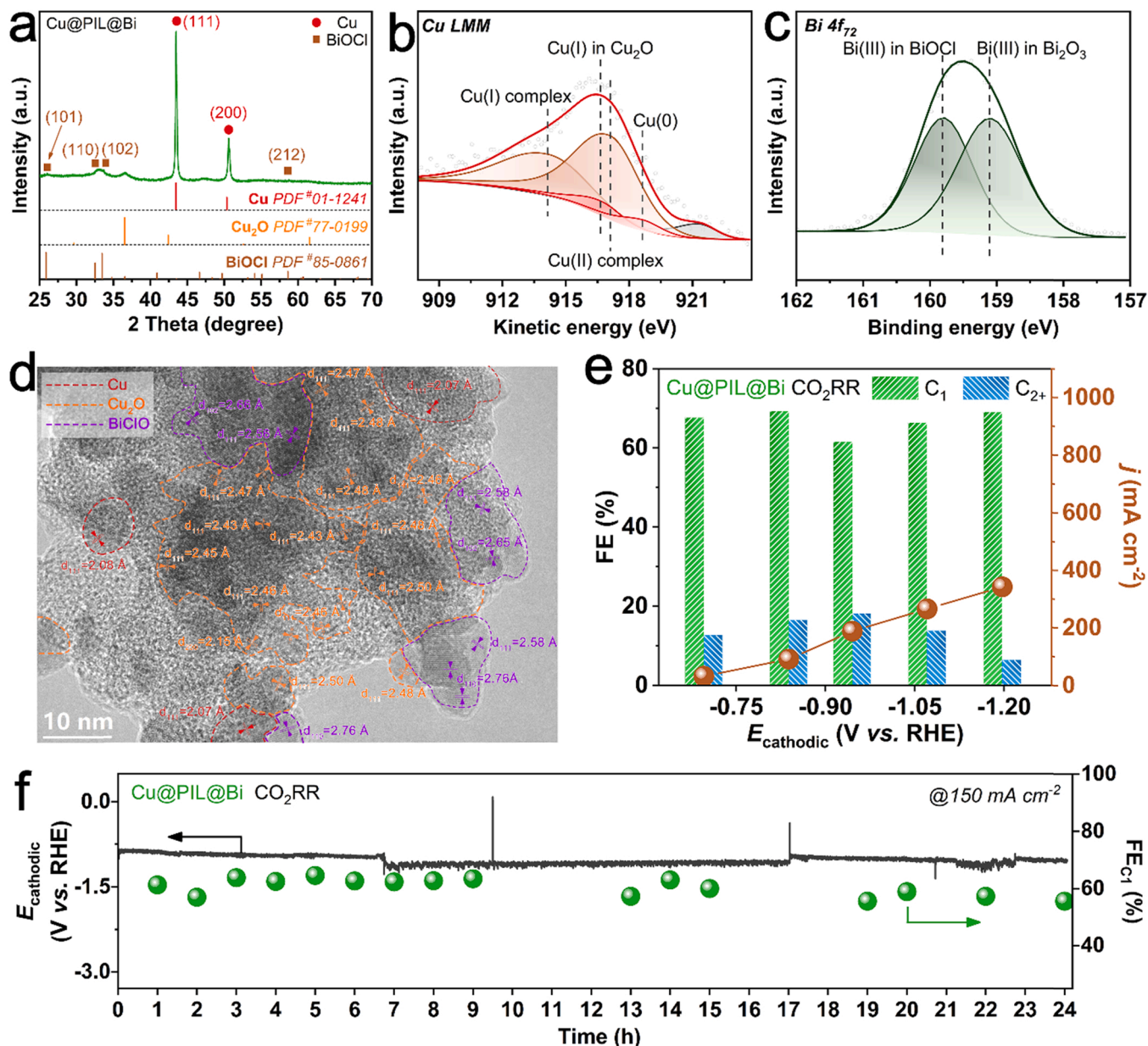


Fig. 4. (a) XRD patterns of Cu@PIL@Bi. (b–c) Cu LMM Auger and Bi $4f_{7/2}$ high-resolution XPS spectra of Cu@PIL@Bi. (d) HR-TEM image of Cu@PIL@Bi (red, orange, and violet dashed lines show fragments of metallic Cu, Cu_2O , and BiOCl, respectively). (e) Electrocatalytic CO_2RR performance of Cu@PIL@Bi in KOH solution (1 M) at different E_{cathodic} . (f) Stability test of Cu@PIL@Bi in KOH solution (1 M) at 150 mA cm^{-2} for 24 h.

Cu-related features, wherein the weak patterns at smaller 2θ degrees (i. e., 25.9° , 32.5° , and 33.5°) are assigned to BiOCl species resulting from the hydrolysis of BiCl_3 during the preparation. The SEM images (Figs. S9 and S10) demonstrate that Cu@PIL@Bi has a similar micromorphology to Cu@PIL@Ag as both hybrid material and catalyst loaded on the GDE. However, the S_{BET} of Cu@PIL@Bi ($199.60 \text{ m}^2 \text{ g}^{-1}$) is higher than that of Cu@PIL@Ag ($183.79 \text{ m}^2 \text{ g}^{-1}$), which is probably attributed to its high proportion of mesoporous (Fig. S11b). On the other hand, XPS spectra (Fig. 4b, c, and S12) suggest that, apart from BiOCl, bismuth also exists in the form of oxides (Bi_2O_3). Further, the coordination interactions between Bi cations, Cl anions, and imidazolium moieties ($\text{Im N}^{\delta+} \dots \text{Cl}^{\delta-} \dots \text{Bi}^{\delta+}$) can be demonstrated by N 1s and Cl 2p spectra (Fig. S12c and d), confirming the presence of interlaced electrostatic interaction networks in the PIL layer of Cu@PIL@Bi. Notably, the diffractive and spectral evidence corresponding to Bi(0) or Bi(V) was not identified, indicating no redox reaction occurs based on bismuth during the impregnation of BiCl_3 . Finally, the HR-TEM image (Figs. 4d and S11a)

shows that nano-sized metallic Cu, Cu_2O , and Bi species (mainly BiOCl) also exist in a highly fragmented manner, signifying plenty of bimetallic phase interfaces (Cu–Bi interfaces) were formed by simply impregnation of metallic compounds without redox reaction. These results suggest that the abundant coordination sites and electrostatic counterparts embedded in the PIL layer are crucial for the high dispersion of extra-introduced metal species, thereby enabling the formation of sufficient and effective phase interfaces for a tandem catalyst.

The electrocatalytic CO_2RR performance of Cu@PIL@Bi was also evaluated in the same electrolyzer with a flowing configuration. As shown in Fig. 4e, j_{total} also increases with the negative shift of E_{cathodic} . However, Cu@PIL@Bi provides a lower j_{total} as compared to Cu@PIL@Ag, suggesting it has worse catalytic activity. In detail, the j_{total} of 91.2 mA cm^{-2} and 135.8 mA cm^{-2} was respectively reached on Cu@PIL@Bi and Cu@PIL@Ag at -0.84 V . Remarkably, Cu@PIL@Bi possesses selectivity mainly towards C_1 products. It maintains a high FE_{C_1} ($> 60\%$) when the E_{cathodic} shifts from -0.70 V to -1.20 V . By

contrast, the FE_{C_2+} varies with $E_{cathodic}$ and the best FE_{C_2+} of 18.1% was reached at -0.95 V with a poor j_{C_2+} of 34.1 mA cm^{-2} . Further, the product distribution profile (Figs. S13 and S14) demonstrates that the major C_1 product is CO at lower overpotential, while it gradually changes to HCOOH at higher overpotential. Meanwhile, the FE_{CH_4} holds a low value ($\sim 3\%$) at $E_{cathodic}$ from -0.70 V to -0.95 V, followed by steadily increases and reaches the potential value of $\sim 15\%$ at -1.07 V (Fig. S13), suggesting a part of *CO is prone to give CH_4 at higher overpotential. In contrast, the FEs of ethylene, ethanol, and acetic acid are low at all the $E_{cathodic}$ s, indicating only a few *CO participate in the C–C coupling to deliver C_{2+} product over Cu@PIL@Bi. Long-term electrolysis suggests the $E_{cathodic}$ slightly negatively shifted from -0.90 V to -1.03 V and the FE_{C_1} decreases from $\sim 60\%$ to $\sim 50\%$ within 24-hour at -150 mA cm^{-2} (Fig. 4f and S15), corresponding to a good stability of Cu@PIL@Bi. Collectively, Cu@PIL@Bi displays a completely different electrocatalytic CO_2RR scenario as compared to Cu@PIL@Ag.

3.4. Electrochemical studies and control experiments

As demonstrated in our previous work, Cu@PIL possesses modest selectivity towards C_{2+} products ($FE_{C_2+} \leq 58\%$) and pure PIL mainly shows hydrogen evolution activity ($FE_{H_2} > 70\%$) [21]. To understand the distinct performance of Cu@PIL@Ag and Cu@PIL@Bi caused by the Cu–Ag and Cu–Bi interfaces, a series of control experiments were carried out. In this regard, Ag-decorated and Bi-decorated PIL materials (denoted as PIL@Ag and PIL@Bi, respectively) were prepared by impregnating AgOAc and BiCl₃ into PIL without the encapsulation of Cu NPs in advance.

PIL@Ag shows the typical AgCl diffraction patterns in the XRD analysis (Fig. S16), corresponding to the ready anion exchange between AgOAc and chloride-based PIL. The presence of AgCl mainly as nano-sized clusters or nanoparticles was further confirmed by Ag 3d_{5/2} XPS spectrum (Fig. S17) and HR-TEM image (Fig. S18). Specifically, it persists two intense peaks at BEs of 369.70 eV and 369.05 eV, which are much higher than that of bulk AgCl (368.10 eV) [35]. The absence of metallic Ag in PIL@Ag strongly supports that the Cu NPs are indispensable in the formation of metallic Ag from AgOAc leading to Cu@PIL@Ag. It agrees well with the galvanic replacement reaction (GRR) mechanism [16] (Eq. 1).



By contrast, XRD patterns and XPS spectra (Figs. S20 and S21) suggest that bismuth presents in the form of varied bismuth oxychlorides in PIL@Bi via coordination and electrostatic interaction. Furthermore, both BiOCl and Bi₂O₃ were observed in PIL@Bi by Bi 4f_{7/2} XPS spectra as that in Cu@PIL@Bi (Figs. 4c and S21b), while the relative amount of BiOCl to Bi₂O₃ in the latter is much less in PIL@Bi. It signifies there is no redox reaction (i.e., no electron transfer) between copper and bismuth during the impregnation, but the presence of Cu NPs may accelerate the hydrolysis of BiCl₃ (Eqs. (2) and (3)). One possibility is that the copper oxides (CuO_x) at the surface of Cu NPs in Cu@PIL@Bi can consume the in-situ generated HCl, thus enabling the hydrolysis of BiCl₃ proceeds forward.



Thermodynamically, the above differences in metal-metal interactions are expected: the redox potential of Ag^+/Ag (0.799 V) is higher than that of Cu^+/Cu (0.520 V) [39], which makes the electron transfer from metal Cu(0) to Ag(I) favorable; however, the redox potential of Bi^{3+}/Bi (0.317 V) [39] are lower than that of Cu^+/Cu , leading to the suppression of electron transfer. Further, the reaction of metallic Cu and Cu₂O with bismuth oxychlorides / oxides are also prohibited based on the thermodynamic calculation (Table S4). SEM images (Figs. S19 and S22) demonstrate that the micromorphology of PIL@Ag

and PIL@Bi is similar to that of Cu@PIL@Ag and Cu@PIL@Bi (Figs. 1d and S9), which are both porous structures composed of stacked spheres with diameters less than 50 nm. Finally, BET tests (Figs. S1b, S11b, and S23) suggest the above four materials possess a similar micro-mesoporous framework to consist of uniform micropores (~ 1.5 nm) and continuous mesopores, which is most likely originated from structural features of the PIL layer.

Electrochemical tests were next conducted to investigate the distinct performance by introducing either AgOAc or BiCl₃ to Cu@PIL. To this end, the previously documented Cu@PIL hybrids by our group [21] are herein cited for comparison. For these metal-PIL hybrids, the conductivity of the PIL layer was envisioned to adjust the barrier for the transfer of charge from the electrolyte solution to the catalytic active sites. The solution resistance (R_s) obtained by electrochemical impedance spectroscopy (EIS) test can therefore be used to estimate the conductivity of the PIL layer when the same electrolyzer and electrolyte solution (e.g., 1 M KOH) are used. As thus, Cu@PIL@Ag (0.75 Ω) and Cu@PIL@Bi (1.13 Ω) both provide much smaller R_s values (Fig. S24) than that of the pristine Cu@PIL (3.23 Ω), suggesting the introduction of metal salts does enhance the conductivity of the PIL layer. Besides, the non-Faradaic double-layer capacitance (C_{dl}) was analyzed by cyclic voltammetry test (Figs. 5a, d, and S25). Evidently, the C_{dl} of both Cu@PIL@Ag (3.37 mF cm^{-2}) and Cu@PIL@Bi (6.34 mF cm^{-2}) are much higher than that of Cu@PIL (1.24 mF cm^{-2}).

Further studies on the R_s and C_{dl} of PIL@Ag and PIL@Bi provide information in-depth. Specifically, the R_s and C_{dl} of PIL@Ag (3.21 Ω and 0.73 mF cm^{-2} , respectively) are close to those of Cu@PIL (3.23 Ω and 1.24 mF cm^{-2} , respectively), which means the improved conductivity and the increased C_{dl} of Cu@PIL@Ag (0.75 Ω and 3.37 mF cm^{-2} , respectively) may not come from a specific domain. In contrast, PIL@Bi persists a low R_s of 0.86 Ω and a high C_{dl} of 8.48 mF cm^{-2} , representing it has better conductivity and higher C_{dl} as compared to both Cu@PIL@Bi (1.13 Ω and 6.34 mF cm^{-2} , respectively) and Cu@PIL (3.23 Ω and 1.24 mF cm^{-2} , respectively). Thus, the electrochemical properties of Cu@PIL@Bi most likely benefit from the PIL@Bi part.

The above viewpoint was further confirmed by linear sweep voltammetry (LSV) curves under different atmospheres (N₂ and CO₂) (Fig. 5b and e). A much better selectivity to CO_2RR over HER was detected on Cu@PIL@Ag as compared to that on either Cu@PIL or PIL@Ag. Meanwhile, Cu@PIL@Ag possesses more positive onset potential for the generation of *H , corresponding to its better capacity in the hydrogenation of different intermediates. However, the corresponding difference between Cu@PIL@Bi, Cu@PIL, and PIL@Bi is not significant. Collectively, the improved electrochemical performance of Cu@PIL@Ag is most likely attributed to the synergistic effect of copper and silver. The GRR of Cu(0) and Ag(I) may account for the observed decreased R_s and increased C_{dl} as compared to those of two independent domains (Cu@PIL and PIL@Ag), which leads to the reconstruction of the Cu-PIL interface and the formation of abundant highly dispersed Cu-Ag interfaces as well as higher ion density embedded in the PIL layer around the active sites. Besides, the Cu-Ag interaction promotes the generation of *CO by facilitating the electron transfer for the formation of *COOH intermediate. By contrast, Cu@PIL@Bi mainly exhibits cumulative properties of two independent domains, namely Cu@PIL and PIL@Bi. It should be due to the absence of electron transfer between copper and bismuth, although Cu@PIL@Bi also processes obvious Cu-Bi interfaces (Fig. 4d).

The CO_2RR performance of PIL@Ag and PIL@Bi was next examined. Evidently, the generation of CO dominates the CO_2RR test over PIL@Ag (Figs. 5c and S26). In contrast, high selectivity to HCOOH was observed by employing PIL@Bi as the electrocatalyst (Figs. 5f and S27). Remarkably, over 50% of FE_{HCOOH} was obtained at all $E_{cathodic}$ s, coincidentally with much poor selectivity to CO ($FE_{CO} < 5\%$). It's worthy to note that both hybrids of PIL@Ag and PIL@Bi cannot accurately represent the "outer" domain of Cu@PIL@Ag and Cu@PIL@Bi based on the full characterization of structure and composition. However, these results

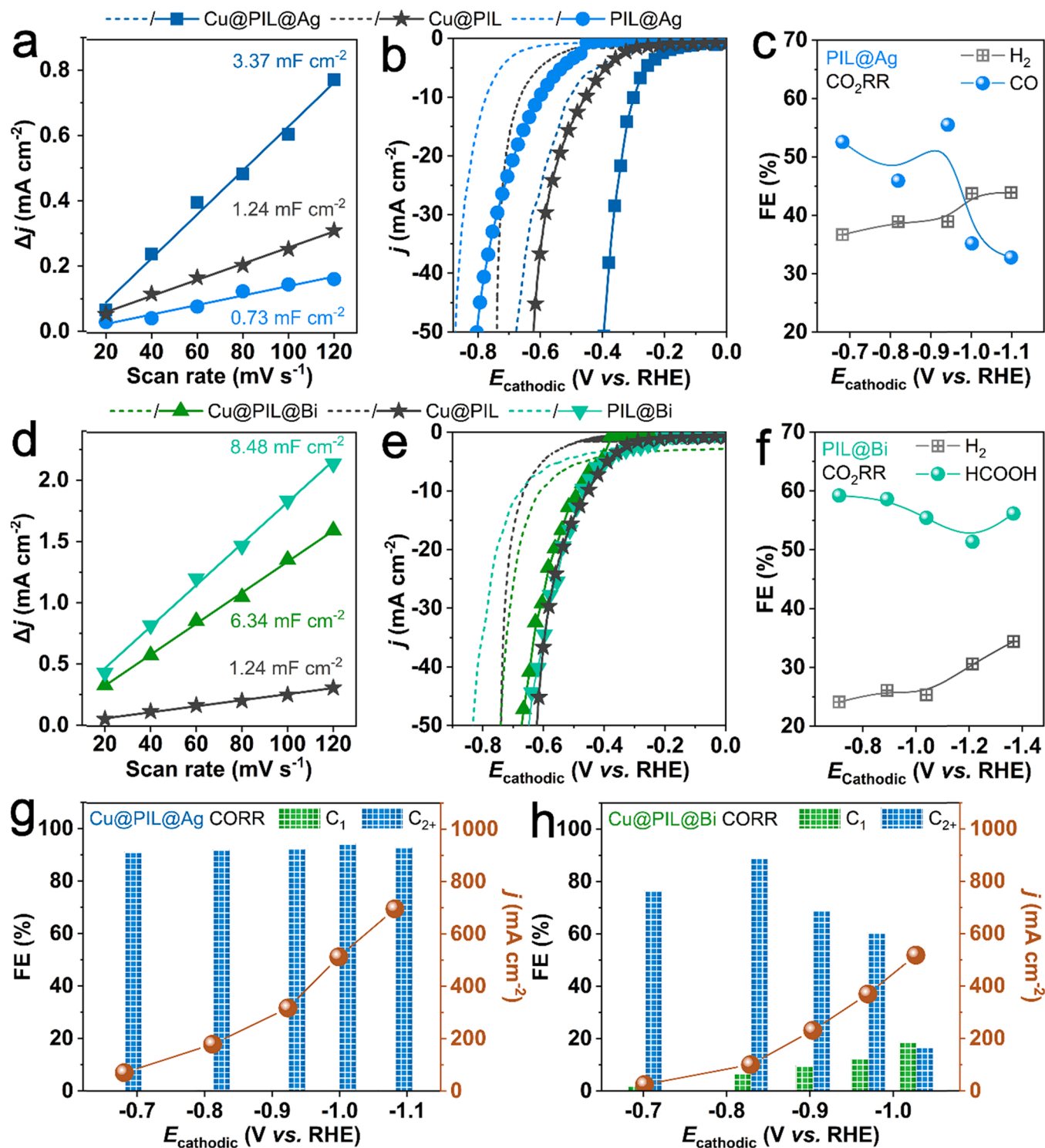


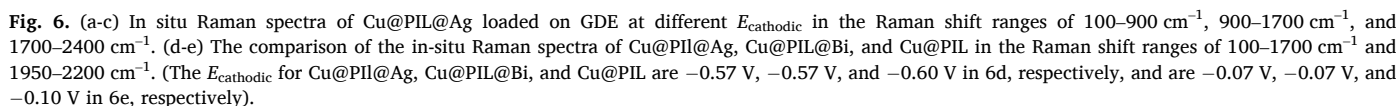
Fig. 5. (a-b) Measured non-Faradaic double-layer capacitance (C_{dl}) and Linear sweep voltammetry (LSV) curves of Cu@PIL@Ag, Cu@PIL, and PIL@Ag. (c) FE and j of H₂ and CO on PIL@Ag in KOH solution (1 M) at different E_{cathodic} . (d-e) C_{dl} and LSV curves of Cu@PIL@Bi, Cu@PIL, and PIL@Bi. (f) FE and j of H₂ and HCOOH on PIL@Bi in KOH solution (1 M) at the different E_{cathodic} . (g-h) Electrocatalytic CORR performance of Cu@PIL@Ag and Cu@PIL@Bi in KOH solution (1 M) at different E_{cathodic} . (in b and e: dashed line represents under N₂ atmosphere; solid line with symbol represents under CO₂ atmosphere).

could demonstrate that the Ag and Bi species in Cu@PIL@Ag and Cu@PIL@Bi account to produce CO and HCOOH, respectively. It agrees well with the recent documents [24,25].

Based on the above discussion, we supposed that the formation of CO is significantly inhibited on Cu@PIL@Bi, resulting in poor C₂₊ selectivity. It's unambiguously demonstrated by CORR experiments, wherein CO gas instead of CO₂ gas was directly supplied. Both Cu@PIL@Ag and

Cu@PIL@Bi display moderate to excellent C₂₊ selectivity. In this case, the different activity and C₂₊ product distribution obtained by these two hybrids correspond to distinct Cu-Ag and Cu-Bi interactions at the surface. For Cu@PIL@Ag (Fig. 5g), a constant high FE_{C₂₊} (> 91%) was obtained at all E_{cathodic} from -0.68 V to -1.08 V, and almost no C₁ products (FE_{C₁} < 1%) was generated. It exhibits a higher selectivity toward ethanol (Fig. S28) compared to CO₂RR (Fig. S3) on the same

(Fig. S31). Besides, the HER dominates the electrocatalysis ($\text{FE}_{\text{H}_2} = 61.1\%$) at higher overpotential (i.e., at -1.03 V). Note that the difference in S_{BET} of two catalysts ($183.79 \text{ m}^2 \text{ g}^{-1}$, and $199.60 \text{ m}^2 \text{ g}^{-1}$) is not significant and the supply mode of the key intermediate (i.e., CO) is the same. Therefore, the distinct performances indicate that Cu@PIL@Ag has the intrinsic nature for promoting C-C coupling and higher



selectivity towards ethanol. The CORR performance of the pristine Cu@PIL was also examined for comparison (Figs. S32 and S33). As a result, the distribution of products on Cu@PIL@Bi rather than Cu@PIL@Ag is quite similar to that on Cu@PIL, signifying the CORR on Cu@PIL@Bi mainly occurs at the Cu-based domain, and however, that on Cu@PIL@Ag is imposed by the synergetic effect of two domains. On the other hand, Cu@PIL@Bi exhibits much lower selectivity towards ethanol than Cu@PIL during CORR (Fig. S33). It confirms the introduction of bismuth to Cu@PIL changed the local chemical environment of Cu sites.

3.5. In situ Raman studies of Cu@PIL@Ag and Cu@PIL@Bi

To study the local chemical environment of active sites and “capture” the intermediates during CO₂RR, the in-situ Raman spectra were conducted on Cu@PIL@Ag and Cu@PIL@Bi. At the open circuit potential (OCP), in addition to Cu₂O-related peaks (513 cm⁻¹ and 626 cm⁻¹) [40], an intense peak at 290 cm⁻¹ and a weak peak at 685 cm⁻¹ are assigned to silver hydroxide (Ag–OH) [41,42] on Cu@PIL@Ag (Figs. 6a and S34). These peaks decay rapidly at E_{cathodic} less than -0.07 V, signifying the copper oxides and silver hydroxides are reduced to Cu(0) and Ag(0) during CO₂RR. Analogously, we suggest that Cu(I) and Cu(II) complexes are reduced during CO₂RR as well. Besides, rapid re-oxidation of both Cu(0) and Ag(0) occurred once the E_{cathodic} was removed (Fig. S34a). A distinct result was obtained on Cu@PIL@Bi despite the quite weak Raman response (Figs. S35 and S36). That is, the bismuth showed obvious characteristics of chlorides and hydroxides after the E_{cathodic} had been removed (Fig. S36c).

To further clarify the composition and structure of electrocatalysts after the electrolysis, comprehensive characterizations of Cu@PIL@Ag and Cu@PIL@Bi after the long-term electrolysis were performed (Figs. S37–S42). Specifically, XRD patterns of the spent Cu@PIL@Ag exhibit unambiguous peaks assigned to the metallic Ag and Cu (Fig. S37). Besides, the diffraction intensity of Cu₂O is stronger than that in fresh Cu@PIL@Ag (Fig. 1a). HR-TEM images (Fig. S38) confirm the presence of Ag, Cu, and Cu₂O. It's worthy to note that many carbon microspheres were found embedded in the PIL layer since the spent Cu@PIL@Ag were scraped from GDE, making it difficult to clearly show the species distribution. In addition, the XPS analysis (Fig. S39) demonstrates that the relative proportion of copper species had remained virtually unchanged and the amount of Cu(II) complex and Cu₂O increased slightly. Further, most of the metallic Ag are still sub nano- to nano-meter-sized. It signifies that the silver species change slightly: only a partial AgOH was reduced in the initial stage of electrolysis, while the rest basically exist in the form of metal before and after the electrolysis.

For the spent Cu@PIL@Bi, only peaks relating to Cu was observed by XRD analysis (Fig. S40), and the bismuth species related peaks are indistinguishable due to the strong background signal from the carbon paper. To our delight, HR-TEM images (Fig. S41) demonstrate the presence of Cu, Bi₂O₃, and BiOCl. Further, the XPS analysis (Fig. S42) suggests more Cu(I) complex and more Bi₂O₃ appeared while other compositions had remained unchanged. In detail, the transformation of bismuth species from oxychlorides/oxides to a mixed states via metallic counterparts (i.e., BiOCl / Bi₂O₃ → Bi(0) → BiOCl / Bi₂O₃ / Bi(OH)₃) occurs for one electrolysis cycle. Furthermore, the XPS spectra in Cl 2p region are weak for both the spent Cu@PIL@Ag and the spent Cu@PIL@Bi due to the ion exchange with OH⁻ anions during the long-term electrolysis, which is consistent with our previous studies [23].

Various vibration modes of intermediates on Cu@PIL@Ag were further identified. For example, in the Raman shift range from 100 cm⁻¹ to 900 cm⁻¹ (Fig. 6a), the *COOH on Ag sites (Ag–COOH) locates at 406 cm⁻¹, while the *OCO⁻ on Ag sites (Ag–OCO⁻) is assigned at 554 cm⁻¹ [43]. The observed low intensity of Ag–COOH peak suggests the kinetics of *CO generation on Ag moiety is fast since *COOH is considered as the precursor leading to *CO [43]. In contrast, the intense peak of Ag–OCO⁻ appears at negative E_{cathodic} over -0.55 V and

maintains until the E_{cathodic} was removed (Fig. S34a). It corresponds to the strong adsorption of *OCO⁻ intermediate by Ag moiety, thereby impeding the formation of HCOOH. Further, the feature peaks at 305 cm⁻¹ and 350 cm⁻¹ for the *CO adsorbed on Cu sites (Cu–CO) [44] are quite weak, signifying the transformation of *CO is very rapid. According to literature [44], the stretching vibration mode of *CO located at ~2000 cm⁻¹. Herein, a broadening of such a peak was observed on Cu@PIL@Ag (2000–2150 cm⁻¹) (Fig. 6c), which is attributed to the presence of many different binding configurations of reaction intermediates containing C–H bonds (i.e., *C_xH_yO₂) [16]. Besides, this peak disappears at negative E_{cathodic} over -0.67 V, corresponding to the accelerated C–C coupling at high overpotential. On Cu@PIL@Bi, the precursor leading to *HCOOH (i.e., *OCHO) was detected at 1283 cm⁻¹, 1440 cm⁻¹, and 1465 cm⁻¹ (Figs. S35 and S36) [45]. More importantly, no spectral feature at ~2000 cm⁻¹ assigned to *CO can be identified on Cu@PIL@Bi (Fig. S35) at all the applied potential, while the *CO adsorbed on Cu sites (Cu–CO) only appears at the potential range from -0.07 V to -0.47 V. It suggests a small population of the key intermediate for C–C coupling (i.e., *CO) presenting on the Cu moiety, which is not sufficient to support the consequent C–C coupling.

The comparison of the in-situ Raman spectra between Cu@PIL@Ag, Cu@PIL@Bi, and Cu@PIL are presented taking two feature ranges of 100–1750 cm⁻² (Fig. 6d) and 1950–2200 cm⁻² as examples (Fig. 6e). In addition to the type and distribution of intermediates, the distinct local chemical environment on these catalysts could also be thus identified. Most remarkable, both Cu@PIL@Ag and Cu@PIL possess plenty of adsorbed surficial copper hydroxides or oxides (i.e., Cu–(OH)_{ad} or Cu–O_{ad}) as demonstrated by the peak at 530 cm⁻¹ [40], but Cu@PIL@Bi does not. Besides, such a peak is relatively stronger on Cu@PIL@Ag than on Cu@PIL. As a result, both Cu@PIL@Ag and Cu@PIL display high performance in the C–C coupling rather than Cu@PIL@Bi [46]. Further, the ready formation of these adsorbed species on Cu@PIL@Ag accounts for the obtained excellent FE_{C₂+} as compared to that on the pristine Cu@PIL. It's essentially attributed to the charge transfer from Cu to Ag [20] and the high local alkalinity induced by multi-electron reduction during CO₂RR. On the other hand, more intense peaks related to the stretching vibration mode of *CO₃²⁻ (857 cm⁻¹ and 1394 cm⁻¹) were detected on Cu@PIL@Bi, suggesting the formation of surficial bismuth carbonates (i.e., (BiO)₂CO₃ or (BiO)₄(OH)₂CO₃) [47]. The intensity of these peaks increases when E_{cathodic} was applied, which however decreases when E_{cathodic} was removed (Figs. S35 and S36). It indicates that the carbonates are adsorbed surficial species formed during the electrocatalysis, which is similar to the adsorbed surficial hydroxides or oxides on copper [40]. A high concentration of such carbon source around the Bi site corresponds to the preferential generation of HCOOH over CO at lower overpotential on Cu@PIL@Bi (Fig. 7d). The assignments of other Raman peaks are summarized in Tables S5 and S6 to give a more detailed analysis.

3.6. DFT calculation and proposed mechanism

To understand the synergic effect between Cu-based domain and Ag-based domain in Cu@PIL@Ag on the CO₂RR leading to both high reaction rate and excellent C₂⁺ selectivity, the density functional theory (DFT) calculations were performed. Herein, to reduce the computational complexity, two key steps, i.e., the generation of *CO intermediate and the C–C coupling reaction, were mainly focused. Correspondingly, two typical interface models (Ag(111)-PIL and Cu(111)-PIL) were constructed to represent active surfaces since both silver and copper present in the metallic state during CO₂RR as demonstrated by the in-situ Raman analysis (Fig. 6).

Evidently, the required free energy leading CO₂ to the *COOH intermediate on Cu(111)-PIL (~0 eV) is much lower than that on Ag(111)-PIL (0.60 eV) (Fig. 7a and Table S7). Besides, such an elementary step proceeds with a higher energy barrier (E_a) on Ag(111)-PIL (1.90 eV) than that on Cu(111)-PIL (1.00 eV), implying the formation of *CO on

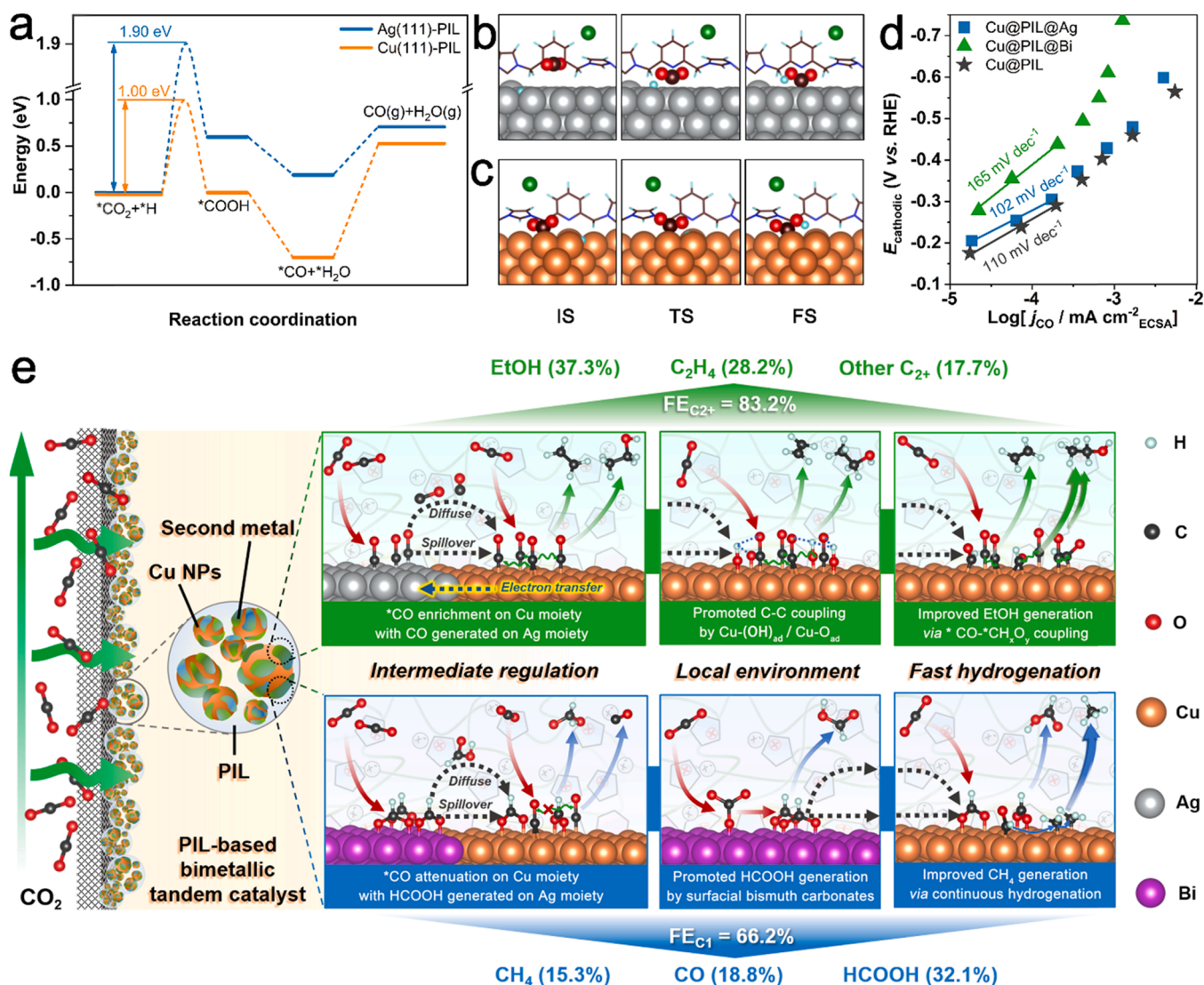


Fig. 7. (a) Energy diagrams of CO_2 to CO on Ag(111)-PIL and Cu(111)-PIL interfaces. (b-c) Optimized structures of initial state (IS), transition state (TS), and final state (FS) of the formation of COOH^* on Ag(111)-PIL and Cu(111)-PIL interfaces. (d) Tafel slopes of Cu@PIL@Ag and Cu@PIL@Bi. (e) The proposed CO_2RR mechanism of Cu@PIL@Ag and Cu@PIL@Bi catalysts. (light blue: H, brown: C, red: O, blue: N, green: Cl, bronze: Cu, gray: Ag, purple: Bi).

Cu is also kinetically favored. The initial state (IS) configuration, transition state (TS) configurations, and final state (FS) configuration during the formation of COOH^* were well optimized (Fig. 7b and c). The subsequent desorption of CO^* from both TM-PIL (TM = Cu(111) and Ag(111)) interfaces is endothermic and independent of the applied potential. Importantly, the calculated higher value on Cu(111)-PIL (+1.37 eV) than that on Ag(111)-PIL (+0.52 eV) suggests the desorption of CO^* from the latter is relatively easier, enabling the spillover and diffusion of CO^* from Ag-based domain to the Cu-based domain.

The C-C coupling step on different domains was next considered. The CHO^* was selected as the synthon due to the high stability of the primary coupling product, namely, the OCHCHO^* intermediate. As shown in Fig. S43, the formation of OCHCHO^* on Ag(111)-PIL interfaces is exothermic with a high free energy value (-1.60 eV). Besides, the E_a of this step is quite low (0.76 eV). In comparison, the free energy variation and E_a of the same C-C coupling on Cu(111)-PIL interface are -0.86 eV and 1.59 eV, respectively, based on our latest calculations [23]. These results suggest the C-C coupling on Ag(111)-PIL is both thermodynamic and kinetic favored as compared with that on Cu(111)-PIL in principle.

Despite these theoretical results, we reasonably proposed that the subsequent C-C coupling mainly occurs on the Cu-based domain

because of the weak adsorption of CO^* on Ag surface as demonstrated by the literature [43] and our calculation (Fig. 7a) and the small proportion of Ag composite in Cu@PIL@Ag. In this regard, the spillover CO^* from Ag to Cu surface and the strong adsorption of CO^* on Cu surface enrich the local concentration of CO^* at the Cu site, enabling a high reaction rate of hydrogenation and C-C coupling. It's worthy to note that the practical CO_2RR mechanism is much more complicated than the focus of this calculation on the C-C coupling. As suggested by our recent results, the specific pathways of generating different C_{2+} products are partially different and involve a variety of possible key intermediates [23]. Further efforts on the theoretical exploration of the detailed mechanism are required in the future.

Tafel analysis was further performed to study the kinetics of transforming CO_2 to CO on Cu@PIL@Ag, Cu@PIL@Bi, and Cu@PIL. As shown in Fig. 7e, Cu@PIL@Ag persists a relatively lower Tafel slope of 102 mV dec⁻¹ as compared to Cu@PIL (110 mV dec⁻¹), suggesting the generation of CO on Cu@PIL@Ag proceeds slightly fast. Besides, a higher overpotential was observed on Cu@PIL@Ag, signifying CO is mainly produced on the Ag moiety. We thus supposed the formation of CO^* on the Ag sites at or near the Cu-Ag interfaces may be significantly accelerated with the assistance of charge transfer from Cu to Ag and

spillover of *CO to Cu sites. By contrast, Cu@PIL@Bi exhibits distinct kinetic behavior, wherein the high Tafel slope of 165 mV dec^{-1} and the small normalized current density demonstrate quite slow kinetics. In this case, such a high slope can be attributed to the mass transport limitation of CO_2 [48]. Based on the experimental results, HCOOH is supposed to be generated on the Bi-based domain, followed by transfer to the surface of the Cu-based domain via diffuse or spillover effect. We speculate that these adsorbed HCOOH (or $HCOO^-$) may cause site blocking, thereby impeding the mass transport of CO_2 to the active sites on the Cu-based domain. Note that our efforts on obtaining the kinetics of HCOOH generation over Cu@PIL@Bi were failed because of the significant quantitative error by the low concentration of liquidus HCOOH under experiments.

Overall, the characteristic of PIL-based bimetallic tandem catalysts was summarized in three points (Fig. 7e): (i) regulating the active sites for various intermediates via both the metal-metal and metal-PIL interactions; (ii) adjusting the local chemical environment through the structure of PIL and the introduced metal elements responsible for specific intermediates generated in-situ; and (iii) improving the supply of *H compatible with the rate of hydrogenating different intermediates.

As confirmed by this study, for the electrolysis of CO_2 on Cu@PIL@Ag, the key *CO intermediate is readily generated at the Cu-based domain. Meanwhile, abundant *CO could be generated on the Ag sites at or near the Cu-Ag interfaces with the assistance of both charge transfer from Cu to Ag [20] and the Ag-PIL interfacial electric field induced by the PIL layer [21]. The local *CO concentration on the Cu sites is thus greatly enriched through the spillover of *CO from the Ag sites (direct path) [16], the re-adsorption of CO caused by the suppression of diffusion by the PIL layer (indirect path) [38], and its high desorption energy of *CO on Cu. Subsequently, the C-C coupling (mainly the $^*CHO-^*CO$ or $^*CHO-^*CHO$ couplings) reactions are significantly enhanced with the promotion of a high population of adsorbed surficial OH imposed by the presence of Ag (Fig. 6) [46], as well as the Cu-PIL interfacial electric field to improve the global C_{2+} selectivity [21]. Furthermore, the presence of Ag-based domain could also accelerate the production of *H (Fig. 5a) [49], thereby facilitating the hydrogenation of *CO to increase the population of *CH_xO_y intermediates. It thus results in the increased FE of ethanol via $^*CO-^*CH_xO_y$ coupling route [17]. For Cu@PIL@Bi, plenty of HCOOH is preferentially produced on the Bi sites at or near the Cu-Bi interfaces with the promotion of “inserted” CO_3^{2-} anions on Bi surface and the PIL-induced interfacial electric field. Next, the in-situ generated HCOOH (or $HCOO^-$) could migrate to the Cu sites by the spillover between two active sites and surface diffusion, leading to the attenuation of *CO intermediates and chemical environment variation at the Cu sites. In this way, the C-C coupling is greatly suppressed because not only the *CO related intermediates are separated but also the active sites for promoting C-C coupling (surficial OH and O species) are absent, thereby delivering HCOOH and CO as the major products. At a higher overpotential, the high local concentration of *H facilitates the continuous hydrogenation of *CO , which promotes the generation of CH_4 on Cu@PIL@Bi. At present, electron transfer between Ag-Cu interaction and Bi-Cu interaction and as well as its influence on CO_2RR performance has been investigated theoretically and experimentally [14,16,18,50]. To get more insight into the metal-metal interactions in the presence of PIL layer and the corresponding CO_2RR mechanism therein, more effort is needed in the future.

4. Conclusions

In summary, two typical PIL-metal-based tandem catalysts, namely, Cu@PIL@Ag and Cu@PIL@Bi, were readily obtained by respectively introducing Ag element with CO-selectivity and Bi element with HCOOH-selectivity to the Cu@PIL hybrids. Remarkably, Cu@PIL@Ag exhibits a high $FE_{C_{2+}}$ of 71.5% with a very high $j_{C_{2+}}$ of 708.9 mA cm^{-2} in 1 M KOH electrolyte solution and an even higher $FE_{C_{2+}}$ of 83.2% with

$j_{C_{2+}}$ of 416.1 mA cm^{-2} in 3 M KOH. Conversely, Cu@PIL@Bi possesses high FE_{C_1} ($> 60\%$) in a wide cathodic potential range. It thus provides a platform to comprehensively study the tandem effect on CO_2RR by the well-developed Cu-based electrocatalysts. Combined theoretical and experimental results suggest the output of such a tandem system, either synergistic or maladjusted, depends on not only the CO_2RR response of the extra metal element (M) but also the specific Cu-M interaction. The presence of the porous PIL layer benefits the facile construction of such bimetallic catalysts, the high dispersion and availability of active sites, and the local enrichment of key intermediates. This contribution provides a facile and universal preparation strategy for the high-throughput screening and systematic study of the tandem effects for high-selectivity and high-speed CO_2RR .

CRediT authorship contribution statement

Xiao-Qiang Li: Data curation, Formal analysis, Visualization, Writing – original draft. **Guo-Yi Duan:** Methodology, Data curation, Formal analysis, Visualization, Writing – original draft. **Rui Wang:** Data curation, Validation. **Li-Jun Han:** Writing – review & editing. **Yao-Feng Wang:** Writing – review & editing. **Bao-Hua Xu:** Conceptualization, Methodology, Writing – review & editing, Supervision, Project administration.

Declaration of Competing Interest

The authors declare that they have no known competing financial interests or personal relationships that could have appeared to influence the work reported in this paper.

Acknowledgments

Financial support from Key Research Program of Frontier Sciences of the Chinese Academy of Sciences (ZDBS-LY-JSC022), Excellent Young Scientists Fund of China (22022815), and National Natural Science Foundation of China (General Program) (U1704251, 21776291) is gratefully acknowledged. We also sincerely appreciate Prof. Suo-Jiang Zhang at IPE for his kind suggestions on the topic.

Appendix A. Supplementary material

Supplementary data associated with this article can be found in the online version at doi:10.1016/j.apcatb.2022.121459.

References

- [1] Y. Li, G. Shi, T. Chen, L. Zhu, D. Yu, Y. Sun, F. Besenbacher, M. Yu, Simultaneous increase of conductivity, active sites and structural strain by nitrogen injection for high-yield CO_2 electro-hydrogenation to liquid fuel, *Appl. Catal. B Environ.* 305 (2022), <https://doi.org/10.1016/j.apcatb.2022.121080>.
- [2] Y. Zou, S. Wang, An investigation of active sites for electrochemical CO_2 reduction reactions: from in situ characterization to rational design, *Adv. Sci.* 8 (2021), 2003579, <https://doi.org/10.1002/advs.202003579>.
- [3] L. Shi, H. Yuan, F. Wu, H. Xia, W. Jiang, C. Yang, G. Hu, Y. Wang, M. Fan, Robust “dry amine” solid CO_2 sorbent synthesized by a facile, cost-effective and environmental friendly pathway, *Chem. Eng. J.* 404 (2021), <https://doi.org/10.1016/j.cej.2020.126447>.
- [4] M. Chu, C. Chen, Y. Wu, X. Yan, S. Jia, R. Feng, H. Wu, M. He, B. Han, Enhanced CO_2 electroreduction to ethylene via strong metal-support interaction, *Green Energy Environ.* (2020), <https://doi.org/10.1016/j.gjee.2020.12.001>.
- [5] K. Ye, T. Liu, Y. Song, Q. Wang, G. Wang, Tailoring the interactions of heterogeneous Ag_2S/Ag interface for efficient CO_2 electroreduction, *Appl. Catal. B Environ.* 296 (2021), <https://doi.org/10.1016/j.apcatb.2021.120342>.
- [6] X. Kang, Q. Zhu, X. Sun, J. Hu, J. Zhang, Z. Liu, B. Han, Highly efficient electrochemical reduction of CO_2 to CH_4 in an ionic liquid using a metal-organic framework cathode, *Chem. Sci.* 7 (2016) 266–273, <https://doi.org/10.1039/C5SC03291A>.
- [7] Y. Kim, S. Park, S.-J. Shin, W. Choi, B.K. Min, H. Kim, W. Kim, Y.J. Hwang, Time-resolved observation of C-C coupling intermediates on Cu electrodes for selective electrochemical CO_2 reduction, *Energy Environ. Sci.* 13 (2020) 4301–4311, <https://doi.org/10.1039/d0ee01690j>.

- [8] D. Zang, Q. Li, G. Dai, M. Zeng, Y. Huang, Y. Wei, Interface engineering of MoS₂/Cu heterostructures toward highly selective electrochemical reduction of carbon dioxide into acetate, *Appl. Catal. B Environ.* 281 (2021), <https://doi.org/10.1016/j.apcatb.2020.119426>.
- [9] C. Chen, Y. Li, S. Yu, S. Louisia, J. Jin, M. Li, M.B. Ross, P. Yang, Cu-Ag tandem catalysts for high-rate CO₂ electrolysis toward multicarbons, *Joule* 4 (2020) 1688–1699, <https://doi.org/10.1016/j.joule.2020.07.009>.
- [10] C.G. Morales-Guio, E.R. Cave, S.A. Nitopi, J.T. Feaster, L. Wang, K.P. Kuhl, A. Jackson, N.C. Johnson, D.N. Abram, T. Hatsukade, C. Hahn, T.F. Jaramillo, Improved CO₂ reduction activity towards C₂₊ alcohols on a tandem gold on copper electrocatalyst, *Nat. Catal.* 1 (2018) 764–771, <https://doi.org/10.1038/s41929-018-0139-9>.
- [11] Z. Li, R.M. Yadav, L. Sun, T. Zhang, J. Zhang, P.M. Ajayan, J. Wu, CuO/ZnO/C electrocatalysts for CO₂-to-C₂₊ products conversion with high yield: on the effect of geometric structure and composition, *Appl. Catal. A Gen.* 606 (2020), <https://doi.org/10.1016/j.apcata.2020.117829>.
- [12] L. Lin, T. Liu, J. Xiao, H. Li, P. Wei, D. Gao, B. Nan, R. Si, G. Wang, X. Bao, Enhancing CO₂ electroreduction to methane with a cobalt phthalocyanine and zinc-nitrogen-carbon tandem catalyst, *Angew. Chem. Int. Ed.* 59 (2020) 22408–22413, <https://doi.org/10.1002/anie.202009191>.
- [13] D. Chen, L.H. Zhang, J. Du, H. Wang, J. Guo, J. Zhan, F. Li, F. Yu, A tandem strategy for enhancing electrochemical CO₂ reduction activity of single-atom Cu-S₁N₃ catalysts via integration with Cu nanoclusters, *Angew. Chem. Int. Ed.* 60 (2021) 24022–24027, <https://doi.org/10.1002/anie.202109579>.
- [14] B. Liu, Y. Xie, X. Wang, C. Gao, Z. Chen, J. Wu, H. Meng, Z. Song, S. Du, Z. Ren, Copper-triggered delocalization of bismuth p-orbital favours high-throughput CO₂ electroreduction, *Appl. Catal. B Environ.* 301 (2022), 120781, <https://doi.org/10.1016/j.apcatb.2021.120781>.
- [15] T. Zhang, Z. Li, J. Zhang, J. Wu, Enhance CO₂-to-C₂₊ products yield through spatial management of CO transport in Cu/ZnO tandem electrodes, *J. Catal.* 387 (2020) 163–169, <https://doi.org/10.1016/j.jcat.2020.05.002>.
- [16] J. Gao, H. Zhang, X. Guo, J. Luo, S.M. Zakeeruddin, D. Ren, M. Gratzel, Selective C-C coupling in carbon dioxide electroreduction via efficient spillover of intermediates as supported by operando raman spectroscopy, *J. Am. Chem. Soc.* 141 (2019) 18704–18714, <https://doi.org/10.1021/jacs.9b07415>.
- [17] A. Herzog, A. Bergmann, H.S. Jeon, J. Timoshenko, S. Kuhl, C. Rettenmaier, M. Lopez Luna, F.T. Haase, B. Roldan Cuenya, Operando investigation of Ag-decorated Cu₂O nanocube catalysts with enhanced CO₂ electroreduction toward liquid products, *Angew. Chem. Int. Ed.* 60 (2021) 7426–7435, <https://doi.org/10.1002/anie.202017070>.
- [18] J. Huang, M. Mensi, E. Oveisi, V. Mantella, R. Buonsanti, Structural sensitivities in bimetallic catalysts for electrochemical CO₂ reduction revealed by Ag-Cu nanodimers, *J. Am. Chem. Soc.* 141 (2019) 2490–2499, <https://doi.org/10.1021/jacs.8b12381>.
- [19] S. Zhang, S. Zhao, D. Qu, X. Liu, Y. Wu, Y. Chen, W. Huang, Electrochemical reduction of CO₂ toward C₂ valuables on Cu@Ag core-shell tandem catalyst with tunable shell thickness, *Small* 17 (2021), e2102293, <https://doi.org/10.1002/smll.202102293>.
- [20] T.T.H. Hoang, S. Verma, S. Ma, T.T. Fister, J. Timoshenko, A.I. Frenkel, P.J. A. Kenis, A.A. Gewirth, Nanoporous copper-silver alloys by additive-controlled electrodeposition for the selective electroreduction of CO₂ to ethylene and ethanol, *J. Am. Chem. Soc.* 140 (2018) 5791–5797, <https://doi.org/10.1021/jacs.8b01868>.
- [21] X.-Q. Li, G.-Y. Duan, J.-W. Chen, L.-J. Han, S.-J. Zhang, B.-H. Xu, Regulating electrochemical CO₂RR selectivity at industrial current densities by structuring copper@poly(ionic liquid) interface, *Appl. Catal. B Environ.* 297 (2021), 120471, <https://doi.org/10.1016/j.apcatb.2021.120471>.
- [22] X.-Q. Li, G.-Y. Duan, X.-X. Yang, L.-J. Han, B.-H. Xu, Electroreduction of carbon dioxide to multi-electron reduction products using poly(ionic liquid)-based Cu-Pd catalyst, *Fundam. Res.* (2022), <https://doi.org/10.1016/j.fmr.2021.12.009>.
- [23] G.Y. Duan, X.Q. Li, G.R. Ding, L.J. Han, B.H. Xu, S.J. Zhang, Highly efficient electrocatalytic CO₂ reduction to C₂₊ products on a poly(ionic liquid)-based Cu⁰-Cu^I tandem catalyst, *Angew. Chem. Int. Ed.* (2021), e202110657, <https://doi.org/10.1002/anie.202110657>.
- [24] D.-D. Ma, S.-G. Han, C. Cao, W. Wei, X. Li, B. Chen, X.-T. Wu, Q.-L. Zhu, Bifunctional single-molecular heterojunction enables completely selective CO₂-to-CO conversion integrated with oxidative 3D nano-polymerization, *Energy Environ. Sci.* 14 (2021) 1544–1552, <https://doi.org/10.1039/d0ee03731a>.
- [25] Q. Gong, P. Ding, M. Xu, X. Zhu, M. Wang, J. Deng, Q. Ma, N. Han, Y. Zhu, J. Lu, Z. Feng, Y. Li, W. Zhou, Y. Li, Structural defects on converted bismuth oxide nanotubes enable highly active electrocatalysis of carbon dioxide reduction, *Nat. Commun.* 10 (2019) 2807, <https://doi.org/10.1038/s41467-019-10819-4>.
- [26] M. Thommes, Physisorption of gases, with special reference to the evaluation of surface area and pore size distribution (IUPAC technical report), *Chem. Int.* 38 (2016), <https://doi.org/10.1515/ci-2016-0119>, 25–25.
- [27] A.C. Miller, G.W. Simmons, Copper by XPS, *Surf. Sci. Spectra* 2 (1993) 55–60, <https://doi.org/10.1116/1.1247725>.
- [28] J.P. Espinós, J. Morales, A. Barranco, A. Caballero, J.P. Holgado, A.R. González-Elipe, Interface effects for Cu, CuO, and Cu₂O deposited on SiO₂ and ZrO₂. XPS determination of the valence state of copper in Cu/SiO₂ and Cu/ZrO₂ catalysts, *J. Phys. Chem. B* 106 (2002) 6921–6929, <https://doi.org/10.1021/jp014618m>.
- [29] M. Finšgar, X-ray excited Auger Cu L₃M_{4,5}M_{4,5} spectra measured at low take-off angles as a fingerprint for a Cu-organics connection, *J. Electron. Spectrosc. Relat. Phenom.* 222 (2018) 10–14, <https://doi.org/10.1016/j.elspec.2017.10.005>.
- [30] J.M. Lázaro Martínez, E. Rodríguez-Castellón, R.M.T. Sánchez, L.R. Denaday, G. Y. Buldain, V. Campo Dall'Orto, XPS studies on the Cu(I,II)-polyampholyte heterogeneous catalyst: an insight into its structure and mechanism, *J. Mol. Catal. A Chem.* 339 (2011) 43–51, <https://doi.org/10.1016/j.molcata.2011.02.010>.
- [31] M.P. Seah, G.C. Smith, M.T. Anthony, AES: Energy calibration of electron spectrometers. I—an absolute, traceable energy calibration and the provision of atomic reference line energies, *Surf. Interface Anal.* 15 (1990) 293–308, <https://doi.org/10.1002/sia.740150503>.
- [32] R. Li, X. Xu, B. Zhu, X.Y. Li, Y. Ning, R. Mu, P. Du, M. Li, H. Wang, J. Liang, Y. Chen, Y. Gao, B. Yang, Q. Fu, X. Bao, In situ identification of the metallic state of Ag nanoclusters in oxidative dispersion, *Nat. Commun.* 12 (2021) 1406, <https://doi.org/10.1038/s41467-021-21552-2>.
- [33] J.Q. Sha, X.Y. Yang, Y. Chen, P.P. Zhu, Y.F. Song, J. Jiang, Fabrication and electrochemical performance of polyoxometalate-based three-dimensional metal organic frameworks containing carbene nanocages, *ACS Appl. Mater. Interfaces* 10 (2018) 16660–16665, <https://doi.org/10.1021/acsami.8b04009>.
- [34] L.J. Gerenser, K.E. Goppert-Berarducci, R.C. Baetzold, J.M. Pochan, The application of photoemission, molecular orbital calculations, and molecular mechanics to the silver-poly(p-phenylene sulfide) interface, *J. Chem. Phys.* 95 (1991) 4641–4649, <https://doi.org/10.1063/1.461733>.
- [35] V.K. Kaushik, XPS core level spectra and Auger parameters for some silver compounds, *J. Electron. Spectrosc. Relat. Phenom.* 56 (1991) 273–277, [https://doi.org/10.1016/0368-2048\(91\)85008-h](https://doi.org/10.1016/0368-2048(91)85008-h).
- [36] B.J. Brisdon, G.F. Griffin, J. Pierce, R.A. Walton, X-ray photoelectron spectra of inorganic molecules, *J. Organomet. Chem.* 219 (1981) 53–59, [https://doi.org/10.1016/0022-328x\(81\)85009-7](https://doi.org/10.1016/0022-328x(81)85009-7).
- [37] J.-K. Sun, Z. Kochovski, W.-Y. Zhang, H. Kirmse, Y. Lu, M. Antonietti, J. Yuan, General synthetic route toward highly dispersed metal clusters enabled by poly(ionic liquids), *J. Am. Chem. Soc.* 139 (2017) 8971–8976, <https://doi.org/10.1021/jacs.7b03357>.
- [38] F.P. García de Arquer, C.-T. Dinh, A. Ozden, J. Wicks, C. McCallum, A.R. Kirmani, D.-H. Nam, C. Gabardo, A. Seifitokaldani, X. Wang, Y.C. Li, F. Li, J. Edwards, L. J. Richter, S.J. Thorpe, D. Sinton, E.H. Sargent, CO₂ electrolysis to multicarbon products at activities greater than 1 A cm⁻², *Science* 367 (2020) 661–666, <https://doi.org/10.1126/science.aay4217>.
- [39] J.G. Speight, *Lange's Handbook of Chemistry*, sixteenth ed., McGraw-Hill, Inc., Laramie, 2004.
- [40] Y. Zhao, X. Chang, A.S. Malkani, X. Yang, L. Thompson, F. Jiao, B. Xu, Speciation of Cu surfaces during the electrochemical CO reduction reaction, *J. Am. Chem. Soc.* 142 (2020) 9735–9743, <https://doi.org/10.1021/jacs.0c02354>.
- [41] E.M. Stuve, R.J. Madix, B.A. Sexton, The adsorption and reaction of H₂O on clean and oxygen covered Ag(110), *Surf. Sci.* 111 (1981) 11–25, [https://doi.org/10.1016/0039-6028\(81\)90471-4](https://doi.org/10.1016/0039-6028(81)90471-4).
- [42] N. Iwasaki, Y. Sasaki, Y. Nishina, Ag electrode reaction in NaOH solution studied by in-situ Raman spectroscopy, *Surf. Sci.* 198 (1988) 524–540, [https://doi.org/10.1016/0039-6028\(88\)90382-2](https://doi.org/10.1016/0039-6028(88)90382-2).
- [43] W. Shan, R. Liu, H. Zhao, Z. He, Y. Lai, S. Li, G. He, J. Liu, In situ surface-enhanced raman spectroscopic evidence on the origin of selectivity in CO₂ electrocatalytic reduction, *ACS Nano* 14 (2020) 11363–11372, <https://doi.org/10.1021/acsnano.0c03534>.
- [44] Z.Z. Niu, F.Y. Gao, X.L. Zhang, P.P. Yang, R. Liu, L.P. Chi, Z.Z. Wu, S. Qin, X. Yu, M. R. Gao, Hierarchical copper with inherent hydrophobicity mitigates electrode flooding for high-rate CO₂ electroreduction to multicarbon products, *J. Am. Chem. Soc.* 143 (2021) 8011–8021, <https://doi.org/10.1021/jacs.1c01190>.
- [45] D. Bohra, I. Ledezma-Yanez, G. Li, W. de Jong, E.A. Pidko, W.A. Smith, Lateral adsorbate interactions inhibit HCOO⁻ while promoting CO selectivity for CO₂ electrocatalysis on silver, *Angew. Chem. Int. Ed.* 58 (2019) 1345–1349, <https://doi.org/10.1002/anie.201811667>.
- [46] G. Iijima, T. Inomata, H. Yamaguchi, M. Ito, H. Masuda, Role of a hydroxide layer on Cu electrodes in electrochemical CO₂ reduction, *ACS Catal.* 9 (2019) 6305–6319, <https://doi.org/10.1021/acscatal.9b00896>.
- [47] P. Taylor, S. Sunder, V.J. Lopata, Structure, spectra, and stability of solid bismuth carbonates, *Can. J. Chem.* 62 (1984) 2863–2873, <https://doi.org/10.1139/v84-484>.
- [48] M. Dunwell, W. Luc, Y. Yan, F. Jiao, B. Xu, Understanding surface-mediated electrochemical reactions: CO₂ reduction and beyond, *ACS Catal.* 8 (2018) 8121–8129, <https://doi.org/10.1021/acscatal.8b02181>.
- [49] X. Gao, Y. Zhou, Z. Cheng, Y. Tan, T. Yuan, Z. Shen, Distance synergy of single Ag atoms doped MoS₂ for hydrogen evolution electrocatalysis, *Appl. Surf. Sci.* 547 (2021), 149113, <https://doi.org/10.1016/j.apsusc.2021.149113>.
- [50] Y.C. Li, Z. Wang, T. Yuan, D.-H. Nam, M. Luo, J. Wicks, B. Chen, J. Li, F. Li, F. Pelayo García de Arquer, Y. Wang, C.-T. Dinh, O. Voznyy, D. Sinton, E. H. Sargent, Binding site diversity promotes CO₂ electroreduction to ethanol, *J. Am. Chem. Soc.* 141 (2019) 8584–8591, <https://doi.org/10.1021/jacs.9b02945>.